iScience

CellPress
OPEN ACCESS

Article

Ion adsorption promotes Frank-van der Merwe growth of 2D transition metal tellurides

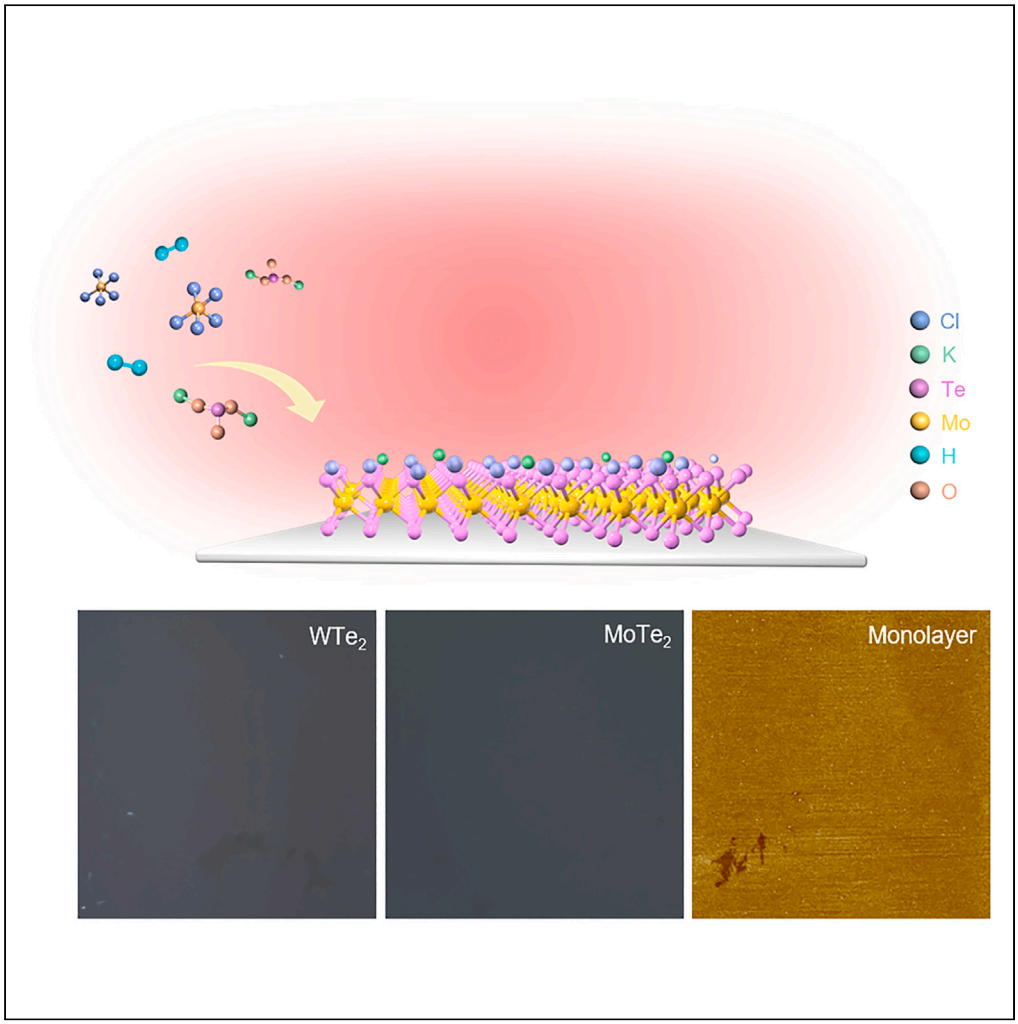

Xingxing Zhang, Jiuxiang Dai, Zhitong Jin, ..., Zemin Zheng, Xianyu Hu, Lin Zhou

linzhou@sjtu.edu.cn

Highlights

Ion adsorption strategy facilitates the Frank-van der Merwe growth

The tellurides exhibit larger sizes, enhanced uniformity, and superior crystallinity

The $MoTe_2$ is stoichiometric and exhibits no discernable oxidation

Zhang et al., iScience 27, 109378
April 19, 2024
https://doi.org/10.1016/j.isci.2024.109378

iScience

CellPress
OPEN ACCESS

Article

Ion adsorption promotes Frank-van der Merwe growth of 2D transition metal tellurides

Xingxing Zhang,[1] Jiuxiang Dai,[1] Zhitong Jin,[1] Xinwei Tao,[1] Yunlei Zhong,[2] Zemin Zheng,[1] Xianyu Hu,[1] and Lin Zhou[1,3,*]

SUMMARY

Reliable synthesis methods for high-quality, large-sized, and uniform two-dimensional (2D) transition-metal dichalcogenides (TMDs) are crucial for their device applications. However, versatile approaches to growing high-quality, large-sized, and uniform 2D transition-metal tellurides are rare. Here, we demonstrate an ion adsorption strategy that facilitates the Frank-van der Merwe growth of 2D transition-metal tellurides. By employing this method, we grow $MoTe_2$ and WTe_2 with enhanced lateral size, reduced thickness, and improved uniformity. Comprehensive characterizations confirm the high quality of as-grown $MoTe_2$. Moreover, various characterizations verify the adsorption of K^+ and Cl^- ions on the top surface of $MoTe_2$. X-ray photoelectron spectroscopy (XPS) analysis reveals that the $MoTe_2$ is stoichiometric without K^+ and Cl^- ions and exhibits no discernable oxidation after washing. This top surface control strategy provides a new controlling knob to optimize the growth of 2D transition-metal tellurides and holds the potential for generalized to other 2D materials.

INTRODUCTION

The scale-up synthesis of high-quality, large-sized, and uniform two-dimensional (2D) transition-metal dichalcogenides (TMDs) is of utmost importance for their device applications, such as nanoelectronics, photonics, and quantum computing.[1–7] To address this requirement, several chemical vapor deposition methods have been developed to facilitate the Frank-van der Merwe growth, enabling layer-by-layer growth of TMDs.[8–10] For instance, strategies such as substrate design to modulate interfacial interactions,[11,12] utilizing organic molecules to promote planar growth,[13,14] and adding salts to enhance precursor vapor pressure and adjust reaction pathways have all been explored.[15–18] While much attention has been given to controlling the underlying surface during TMD growth, manipulating the top surface presents a novel avenue for promoting the Frank-van der Merwe growth. A breakthrough has been achieved by employing a MoS_2-OH bilayer approach to fabricate inch-sized monolayer MoS_2 on various substrates.[19] However, effectively controlling the top surface is rare and remains challenging, as absorption and growth need to coincide at the same location.

2D transition-metal tellurides have garnered significant attention due to their unique physicochemical properties and promising applications.[20–24] For instance, 2H and 1T′ $MoTe_2$ can be synthesized and integrated simultaneously in a single step, creating high-performance 2D devices.[25,26] Additionally, 1T′-WTe_2 exhibits spontaneous ferroelectric switching, challenging the conventional notion that ferroelectric properties cannot exist in metallic systems.[27,28] Consequently, there is a pressing need to obtain large crystal sizes and uniform 2D transition-metal tellurides. However, most existing methods primarily focus on 2D transition-metal sulfides and selenides,[18,29,30] leaving a dearth of versatile approaches for growing large-sized and uniformly layered 2D transition-metal tellurides.

In this study, we have developed an ion absorption method to promote the Frank-van der Merwe growth of 2D transition-metal tellurides. Our approach enables the synthesis of $MoTe_2$ with enhanced quality, larger sizes, reduced thickness, and improved uniformity when compared to growth without this method. Moreover, we have grown uniform monolayer $MoTe_2$ and WTe_2 films by extending the growth time. The growth process involves simultaneous $MoTe_2$ formation, K^+ ion absorption, and Cl^- ion adsorption at the growth site. These ions impede vertical growth while promoting the Frank-van der Merwe growth of 2D transition-metal tellurides. This ion adsorption-enabled top surface tuning offers a novel strategy for synthesizing large-sized and uniform 2D metal tellurides, potentially applicable to other 2D TMDs.

[1]School of Chemistry and Chemical Engineering, Frontiers Science Centre for Transformative Molecules, Shanghai Jiao Tong University, Shanghai 200240, China
[2]Key Laboratory of Multifunctional Nanomaterials and Smart Systems, Division of Advanced Materials, Suzhou Institute of Nano-Tech and Nano-Bionics, Chinese Academy of Sciences, Suzhou 215123, China
[3]Lead contact
*Correspondence: linzhou@sjtu.edu.cn
https://doi.org/10.1016/j.isci.2024.109378

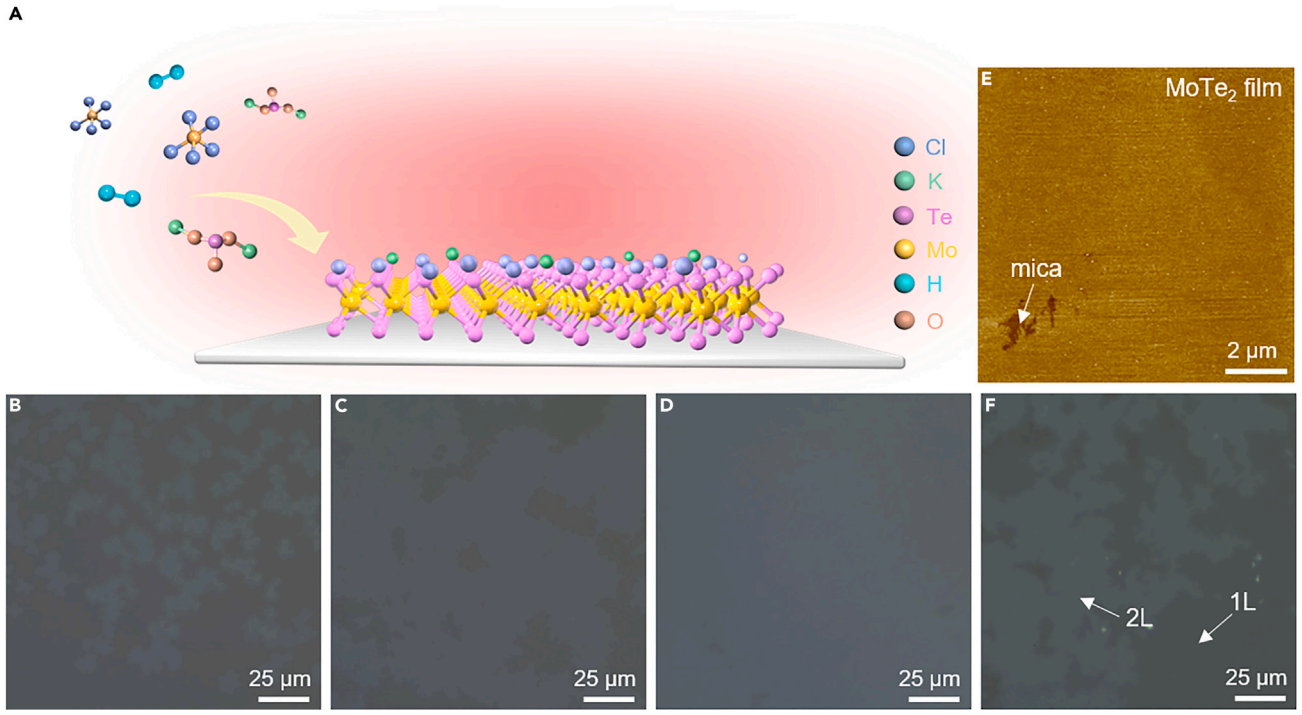

Figure 1. The schematic diagram and optical image of the $MoTe_2$ synthesis process

(A) The schematic diagram of the ion adsorption promoted $MoTe_2$ synthesis.

(B–D) Typical optical microscopy (OM) image of CVD-grown $MoTe_2$ under 1 min (B), 3 min (C), and 5 min (D).

(E) AFM image of CVD-grown monolayer $MoTe_2$ film.

(F) Typical optical microscopy (OM) image of CVD-grown $MoTe_2$ under 6 min.

RESULTS AND DISCUSSION

In our experimental design, we employ K_2TeO_3 and $MoCl_5$ as precursors to grow $MoTe_2$ and generate K^+ and Cl^- ions simultaneously. To ensure optimal and homogeneous dispersion of K_2TeO_3, we initially dissolved K_2TeO_3 powder in deionized water. Subsequently, the K_2TeO_3 solution is spin-coated onto fluorophlogopite mica. The excellent hydrophilicity of freshly cleaved mica facilities the even dispersion of K_2TeO_3 on mica. The deposited K_2TeO_3 is then dehydrated at 60°C, leading to its drying and immobilization on mica substrate (Figure S1). During the growth process, the predeposited K_2TeO_3 vaporizes and reacts with the metal chloride precursor at the growth temperature. The chemical reaction equation for growing $MoTe_2$ can be represented as:

$$2MoCl_5+4K_2TeO_3+13H_2 \rightarrow 2MoTe_2+8KCl+12H_2O+2HCl$$

Importantly, the generation of ions and the growth of $MoTe_2$ occur simultaneously at the same location (Figure 1A). After a brief period of growth, uniform monolayer $MoTe_2$ flakes emerge on mica substrate (Figure 1B). As growth time prolongs, monolayer flakes continue to grow without the appearance of thicker flakes (Figure 1C). With further extension of time, dispersed monolayer $MoTe_2$ flakes merge to form a continuous and uniform $MoTe_2$ film (Figure 1D). Atomic force microscopy (AFM) analysis reveals that the thickness of the film is ~0.73 nm with slight roughness (~0.12 nm), indicating a smooth monolayer $MoTe_2$ film (Figure 1E).

The morphology of synthesized $MoTe_2$ is highly influenced by the growth temperature and growth time (Figure S2). Scattered monolayer $MoTe_2$ flakes are grown at 600°C. As the reaction temperature rises, the crystal size of $MoTe_2$ gradually increases. At 650°C, a relatively uniform monolayer $MoTe_2$ film is obtained, exhibiting a lateral dimension that reaches the millimeter scale. Further raising the growth temperature results in the uniform growth of a second layer of $MoTe_2$ on the monolayer film (Figure S2). Moreover, the second layer $MoTe_2$ flakes grows on the monolayer film when increasing the growth time (Figure 1F). These observations strongly suggest that the growth mode in our method follows the Frank-van der Merwe growth,[31] characterized by a layer-by-layer deposition process.

K_2TeO_3 is crucial for achieving large-sized and uniform 2D $MoTe_2$. To investigate the role of K_2TeO_3, we conducted growth experiments without K_2TeO_3 while keeping all other growth parameters identical. The absence of K_2TeO_3 results in small $MoTe_2$ flakes with a wide thickness distribution (Figure 2A). The lateral size of flakes falls within the range of 10–20 μm. Their thicknesses vary from 0.7 nm to 25 nm. In contrast, larger-sized and uniform $MoTe_2$ flakes are obtained by introducing K_2TeO_3 (Figure 2B). Uniform monolayer $MoTe_2$ flakes are grown, as evidenced by the thickness of ~0.73 nm (Figure 2C). The thickness distribution is concentrated below 5 nm (Figure 2D), indicating that

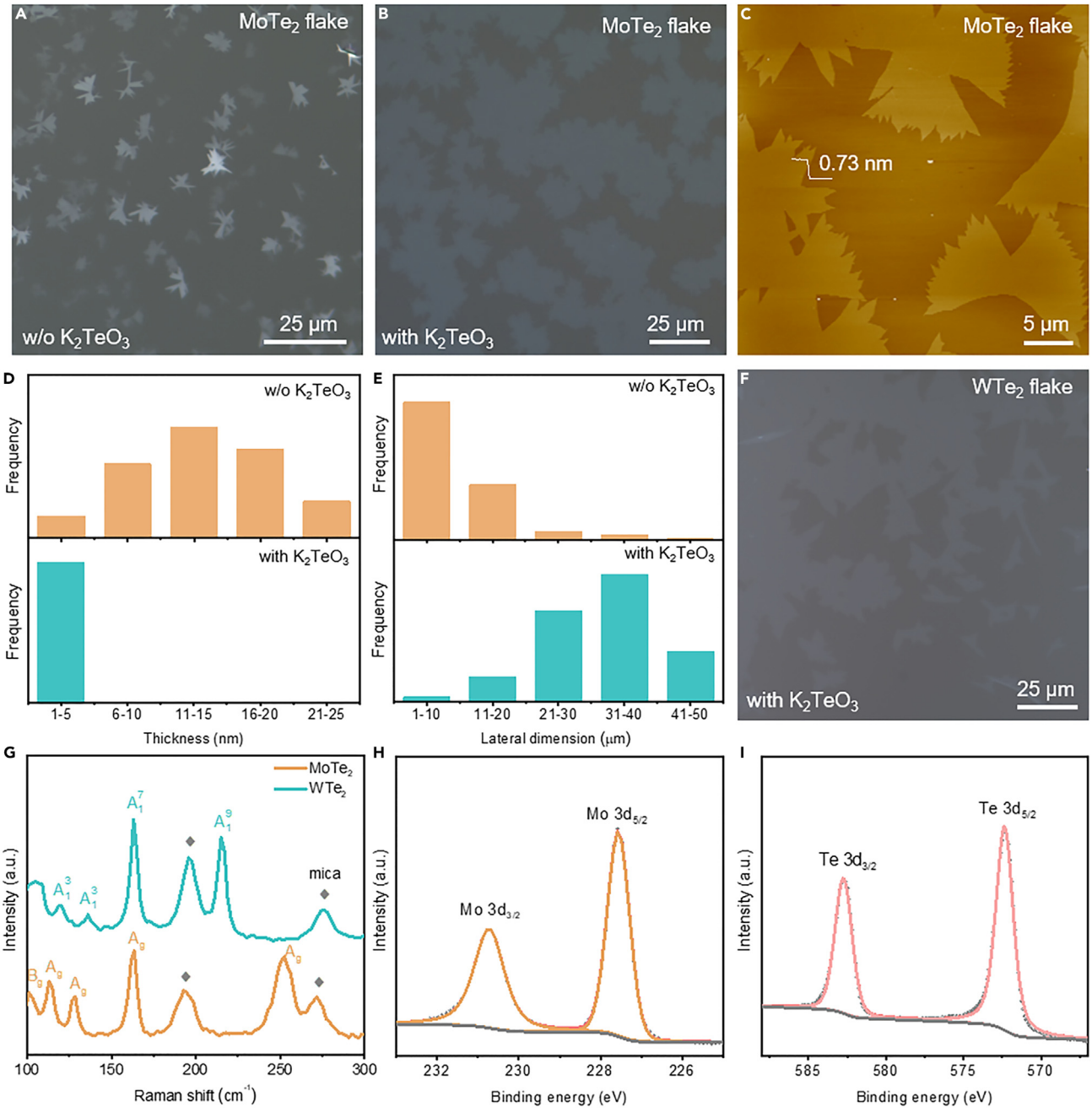

Figure 2. Characterizations of CVD-grown $MoTe_2$ and WTe_2

(A) Optical image of $MoTe_2$ grown without K_2TeO_3.

(B) Optical image of $MoTe_2$ film grown with K_2TeO_3.

(C) AFM image of CVD-grown $MoTe_2$ flake.

(D and E) Thickness and lateral dimension distribution analysis of $MoTe_2$ flakes.

(F) Optical image of WTe_2 film grown with K_2TeO_3.

(G) Raman spectra of CVD-grown $MoTe_2$ and WTe_2 flakes on mica substrate.

(H and I) High-resolution XPS spectra of Mo 3 days (H) and Te 3 days (I) in $MoTe_2$.

K_2TeO_3 effectively reduces the thickness and thickness variation of $MoTe_2$. Notably, with the addition of K_2TeO_3, $MoTe_2$'s lateral size increases to approximately 30–50 μm, demonstrating the efficient promotion of lateral growth (Figure 2E). The quantity of K_2TeO_3 is important for the growth of $MoTe_2$. Inadequate K_2TeO_3 do not exhibit a noticeable impact on the $MoTe_2$ growth. Conversely, excessive K_2TeO_3 impede

the growth of large-sized and uniform monolayer $MoTe_2$ (Figure S2). Furthermore, the Raman spectrum of as-grown $MoTe_2$ with K_2TeO_3 shows characteristic peaks at 102, 115, 130, 161, and 252 cm^{-1}, corresponding to monolayer 1T′-$MoTe_2$.[32,33] The sharp peak with a full width at half-maximum (FWHM) of 6.3 cm^{-1} at the representative A_g mode (161 cm^{-1}) suggests the high crystallinity of monolayer 1T′-$MoTe_2$ (Figure 2G).[33]

Our strategy for $MoTe_2$ growth through ion adsorption is also effective for the growth of WTe_2 (Figures 2F and S3). Similarly, the absence of predeposited K_2TeO_3 leads to small and nonuniform WTe_2 flakes (Figure S3). In contrast, introducing K_2TeO_3 results in large-sized and uniform WTe_2 flakes (Figures 2F and S3). Moreover, distinct Raman active A_1 modes corresponding to WTe_2 are observed at 114, 132, 161, and 209 cm^{-1}, consistent with the previous reports on monolayer 1T′-WTe_2 (Figure 2G).[34,35]

A series of characterizations verify the high quality of as-grown $MoTe_2$. X-ray photoelectron spectroscopy (XPS) survey spectrum reveals prominent Mo and Te peaks, while no discernible K or Cl peaks, indicating the CVD sample is free of K^+ and Cl^- ions contamination after water washing treatment (Figure S4). Two prominent peaks located at 227.5 (Mo $3d_{5/2}$) and 230.5 eV (Mo $3d_{3/2}$) correspond to Mo-Te bonds (Figure 2H). The Te $3d_{5/2}$ and Te $3d_{3/2}$ peaks at 572.8 and 582.6 eV are also assigned to Mo-Te bonds (Figure 2I). Furthermore, the atomic ratio between Mo and Te is approximately 1:2, suggesting that the CVD-grown $MoTe_2$ is stoichiometric. All these features are consistent with previous XPS results for 1T′-$MoTe_2$.[33,34] Notably, both Mo 3 days and Te 3 days spectra show no discernable oxidation peaks related to Mo-O or Te-O bonds. This observation suggests that the as-grown $MoTe_2$ exhibits high resistance to degradation in ambient conditions, thus reflecting the high crystal quality of our $MoTe_2$ sample.

The high quality of as-synthesized $MoTe_2$ and WTe_2 can be further confirmed by transmission electron microscopy (TEM) and polarized Raman spectroscopy. The selected area electron diffraction pattern (SAED) taken on $MoTe_2$ flake shows a single set of rectangle patterns, consistent with the feature of monoclinic phase $MoTe_2$ (Figure 3B). High-resolution TEM (HRTEM) image reveals a nearly perfect periodic atom arrangement with a lattice spacing of 0.63 nm, corresponding to the (100) planes of $MoTe_2$ (Figure 3A).[33,36] The perfect lattice without noticeable defects suggests high quality of as-grown $MoTe_2$. The SAED of WTe_2 flake also displays a single set of rectangle patterns, corresponding to 1T′-WTe_2 (Figure S5). Moreover, 2D mapping of different vibration modes confirms strong in-plane anisotropy of $MoTe_2$ and WTe_2 (Figures 3F and S7). The corresponding polar plots of different vibration modes are depicted in Figures 3G, S6, and S7. The polar plot of Raman peak intensity at 161 cm^{-1} shows a typical two-lobe pattern, indicating the Raman anisotropy of the $MoTe_2$ with 2-fold symmetry (Figure 3G). The maximum intensity direction (marked with yellow double arrows) of the A_g mode peaks corresponds to the Mo-Te chain direction.[37,38]

The homogeneity of $MoTe_2$ and WTe_2 are evaluated through energy dispersive spectroscopy (EDS) and Raman mapping. EDS spectrum confirms the presence of Mo (W) and Te elements in the $MoTe_2$ (WTe_2) sample, without any detectable elemental impurities (Figure S8). Elemental maps demonstrate uniform colors across the flake region, indicating a homogeneous spatial distribution of both Te and Mo (W) elements (Figures 3C–3E and S5). Furthermore, Raman intensity maps at 161 cm^{-1} (Figures 3H and 3I) display uniformly distributed color across the flake, indicating the uniformity of as-grown $MoTe_2$.

To verify the ion adsorption growth of $MoTe_2$, we conducted XPS and time-of-flight secondary ion mass spectrometry (TOF-SIMS) on as-grown monolayer $MoTe_2$ (Figure 4A). XPS fine-scan spectra exhibit Cl and K peaks, indicating the existence of K^+ and Cl^- ions in the $MoTe_2$ sample (Figures 4B and 4C). Moreover, we identify ions distribution of the $MoTe_2$ sample using TOF-SIMS in negative modes. Low-resolution cross-sectional images (Figures 4D–4F) demonstrate that Cl^- and KCl^- ions locate above Te^- ion, suggesting K^+ and Cl^- ions adsorb on the top surface of monolayer $MoTe_2$ during growth. 3D images of depth profiles (Figures 4G and 4H) visually represent the vertical distribution patterns of Cl^- and KCl^-. Furthermore, the normalized TOF-SIMS depth profile indicates that the Cl, K, Te, Mo, and Al ions (from mica substrate) are distributed from top to bottom, verifying K^+ and Cl^- ions adsorption on the top surface of monolayers $MoTe_2$ (Figure 4I). In contrast to conventional methods that rely on promoting in-plane growth to inhibit vertical growth and achieve uniform monolayers, we present a novel approach utilizing surface ion adsorption to suppress vertical growth and facilitate in-plane growth. This approach offers improved control over the thickness and uniformity of 2D transition metal tellurides.

Conclusions

In summary, we have developed an ion adsorption method to promote the Frank-van der Merwe growth of 2D transition metal tellurides. Through this method, the as-grown transition metal tellurides exhibit notable improvements, including larger sizes, reduced thickness, and enhanced uniformity compared to those grown without this technique. Moreover, the as-grown $MoTe_2$ exhibits stoichiometric composition, superior crystallinity, and homogeneity. This research broadens the synthesis methods for achieving high-quality, large-sized, and uniform 2D transition metal tellurides. We anticipate this tuning top surface strategy can be generalized to synthesizing other 2D materials.

Limitations of the study

We have developed an ion adsorption method to promote uniform growth of two-dimensional layered materials. However, the applicability of ion adsorption in synthesizing non-layered materials remains unexplored, which also serves as our future research direction.

STAR★METHODS

Detailed methods are provided in the online version of this paper and include the following:

- KEY RESOURCES TABLE
- RESOURCE AVAILABILITY

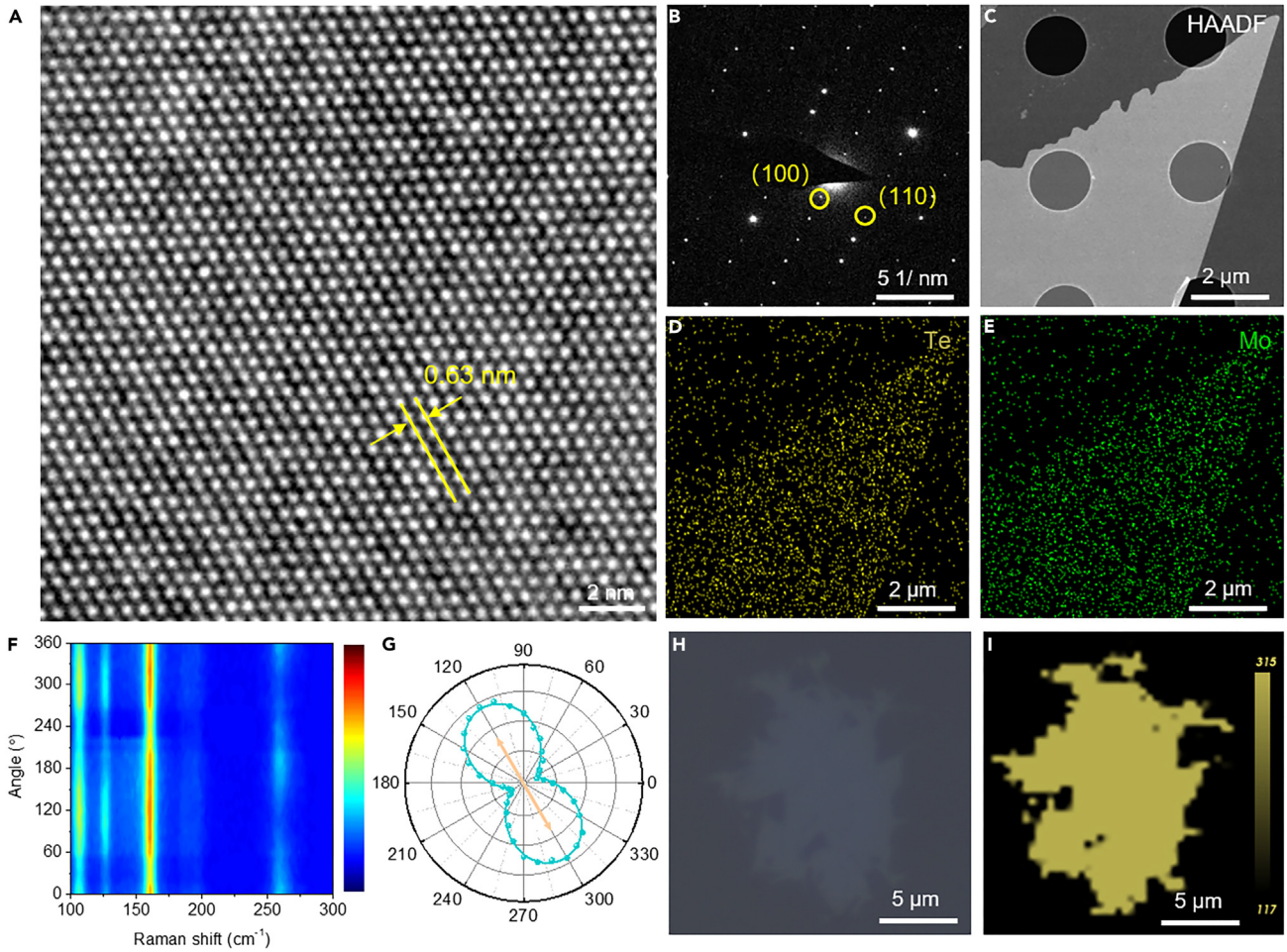

Figure 3. TEM and Raman characterization of $MoTe_2$ grown with K_2TeO_3

(A) High-resolution TEM image of a $MoTe_2$ flake.

(B) SAED pattern of a $MoTe_2$ flake.

(C–E) HAADF-TEM image of a $MoTe_2$ flake and corresponding EDS element mapping of Te and Mo elements.

(F) 2D mapping of Raman spectra regarding the incident light's polarization angle (θ).

(G) Polar plots for the Raman peak intensity at 161 cm^{-1} with respect to θ.

(H and I) Optical image of $MoTe_2$ flake and corresponding Raman intensity map of the 161 cm^{-1} peaks.

SUPPLEMENTAL INFORMATION

Supplemental information can be found online at https://doi.org/10.1016/j.isci.2024.109378.

ACKNOWLEDGMENTS

We thank Prof. Qinghong Yuan for the helpful discussion. This work was supported by the National Key Basic R&D Program of China (2021YFA1401400), the National Natural Science Foundation of China (52103344), the China Postdoctoral Science Foundation (2023M742557) and the Jiangsu Funding Program for Excellent Postdoctoral Talent (2023ZB167).

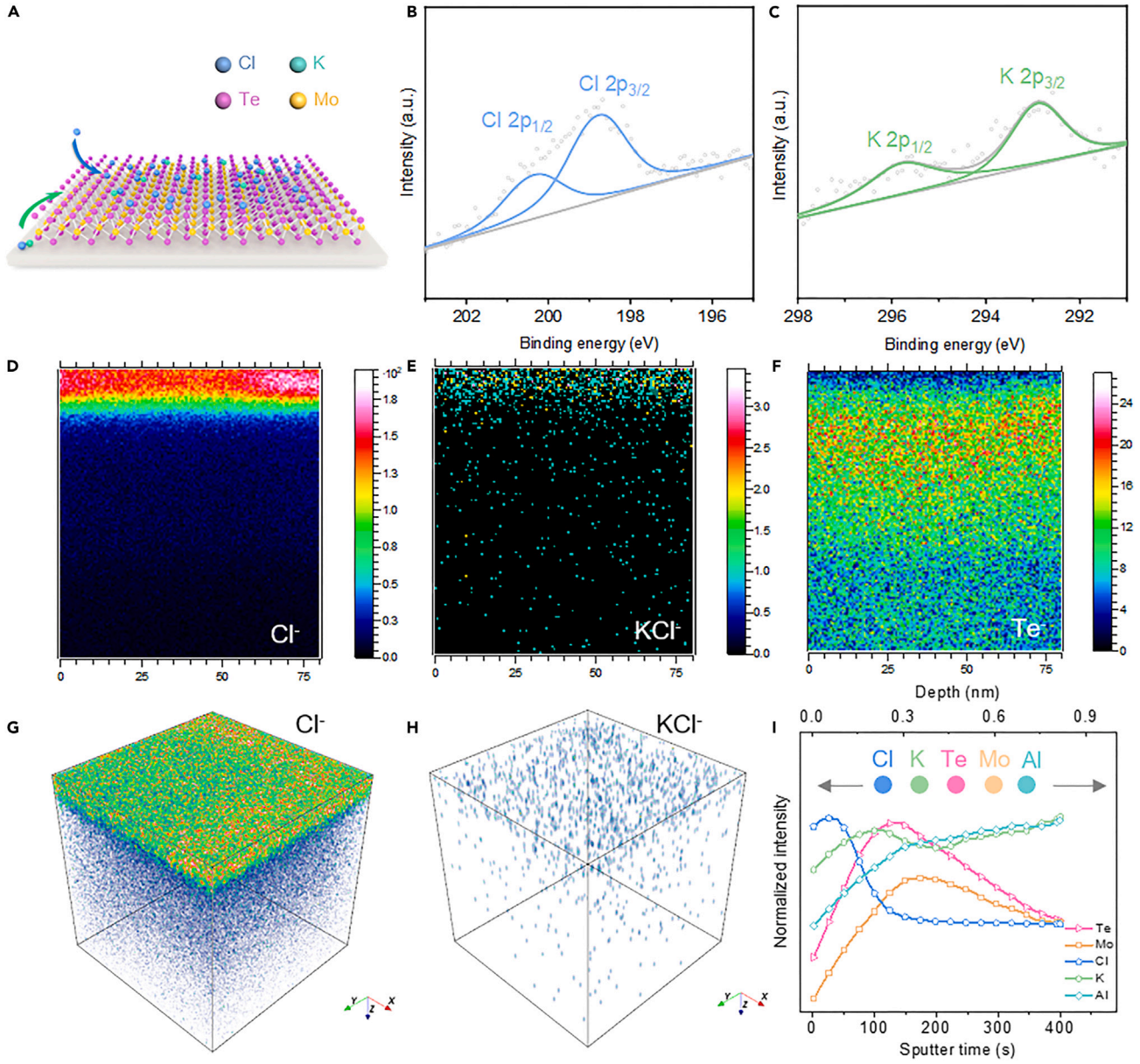

Figure 4. XPS and TOF-SMIS characterizations of $MoTe_2$ grown with K_2TeO_3

(A) Schematic diagrams of CVD-grown $MoTe_2$ with Cl^- and K^+ ions on mica substrate.

(B and C) High-resolution XPS spectra of $MoTe_2$ with Cl (B) and K (C) elements in Si/SiO_2 substrate.

(D–F) Low-resolution cross-section image of Cl^-, KCl^-, and Te^-.

(G and H) Low-resolution 3D image of Cl^- and KCl^-.

(I) Normalized TOF-SIMS depth profile of the $MoTe_2$ sample.

AUTHOR CONTRIBUTIONS

X.X.Z. and L.Z. conceived this work. X.X.Z. carried out the experiments of 2D tellurides growth. X.X.Z., J.X.D., Z.T.J., X.W.T., Y.L.Z., Z.M.Z., and X.Y.H. participated in the material characterizations. J.X.D., Z.T.J., and Z.M.Z. provided suggestions and assistance in data analysis. All authors discussed the results and commented on the manuscript.

DECLARATION OF INTERESTS

The authors declare no competing interests.

Received: December 28, 2023
Revised: January 30, 2024
Accepted: February 27, 2024
Published: March 2, 2024

REFERENCES

1. Hou, W., Azizimanesh, A., Sewaket, A., Peña, T., Watson, C., Liu, M., Askari, H., and Wu, S.M. (2019). Strain-based room-temperature non-volatile $MoTe_2$ ferroelectric phase change transistor. Nat. Nanotechnol. *14*, 668–673. https://doi.org/10.1038/s41565-019-0466-2.
2. Bie, Y.Q., Grosso, G., Heuck, M., Furchi, M.M., Cao, Y., Zheng, J., Bunandar, D., Navarro-Moratalla, E., Zhou, L., Efetov, D.K., et al. (2017). A $MoTe_2$-based light-emitting diode and photodetector for silicon photonic integrated circuits. Nat. Nanotechnol. *12*, 1124–1129. https://doi.org/10.1038/nnano.2017.209.
3. Song, P., Hsu, C.-H., Vignale, G., Zhao, M., Liu, J., Deng, Y., Fu, W., Liu, Y., Zhang, Y., Lin, H., et al. (2020). Coexistence of large conventional and planar spin Hall effect with long spin diffusion length in a low-symmetry semimetal at room temperature. Nat. Mater. *19*, 292–298. https://doi.org/10.1038/s41563-019-0600-4.
4. Manzeli, S., Ovchinnikov, D., Pasquier, D., Yazyev, O.V., and Kis, A. (2017). 2D transition metal dichalcogenides. Nat. Rev. Mater. *2*, 17033. https://doi.org/10.1038/natrevmats.2017.33.
5. Han, G.H., Duong, D.L., Keum, D.H., Yun, S.J., and Lee, Y.H. (2018). Van der waals metallic transition metal dichalcogenides. Chem. Rev. *118*, 6297–6336. https://doi.org/10.1021/acs.chemrev.7b00618.
6. Qian, X., Liu, J., Fu, L., and Li, J. (2014). Quantum spin Hall effect in two-dimensional transition metal dichalcogenides. Science *346*, 1344–1347. https://doi.org/10.1126/science.1256815.
7. Ma, T., Chen, H., Yananose, K., Zhou, X., Wang, L., Li, R., Zhu, Z., Wu, Z., Xu, Q.-H., Yu, J., et al. (2022). Growth of bilayer $MoTe_2$ single crystals with strong non-linear Hall effect. Nat. Commun. *13*, 5465. https://doi.org/10.1038/s41467-022-33201-3.
8. Zhang, T., Wang, J., Wu, P., Lu, A.-Y., and Kong, J. (2023). Vapour-phase deposition of two-dimensional layered chalcogenides. Nat. Rev. Mater. *8*, 799–821. https://doi.org/10.1038/s41578-023-00609-2.
9. Liu, C., Wang, L., Qi, J., and Liu, K. (2020). Designed growth of large-size 2D single crystals. Adv. Mater. *32*, e2000046. https://doi.org/10.1002/adma.202000046.
10. Kim, S.Y., Kwak, J., Ciobanu, C.V., and Kwon, S.Y. (2019). Recent developments in controlled vapor-phase growth of 2D group 6 transition metal dichalcogenides. Adv. Mater. *31*, 1804939. https://doi.org/10.1002/adma.201804939.
11. Yang, P., Zou, X., Zhang, Z., Hong, M., Shi, J., Chen, S., Shu, J., Zhao, L., Jiang, S., Zhou, X., et al. (2018). Batch production of 6-inch uniform monolayer molybdenum disulfide catalyzed by sodium in glass. Nat. Commun. *9*, 979. https://doi.org/10.1038/s41467-018-03388-5.
12. Han, S.S., Ko, T.-J., Yoo, C., Shawkat, M.S., Li, H., Kim, B.K., Hong, W.-K., Bae, T.-S., Chung, H.-S., Oh, K.H., and Jung, Y. (2020). Automated assembly of wafer-scale 2D TMD heterostructures of arbitrary layer orientation and stacking sequence using water dissoluble salt substrates. Nano Lett. *20*, 3925–3934. https://doi.org/10.1021/acs.nanolett.0c01089.
13. Ling, X., Lee, Y.-H., Lin, Y., Fang, W., Yu, L., Dresselhaus, M.S., and Kong, J. (2014). Role of the seeding promoter in MoS_2 growth by chemical vapor deposition. Nano Lett. *14*, 464–472. https://doi.org/10.1021/nl4033704.
14. Lee, Y.-H., Zhang, X.-Q., Zhang, W., Chang, M.-T., Lin, C.-T., Chang, K.-D., Yu, Y.-C., Wang, J.T.-W., Chang, C.-S., Li, L.-J., and Lin, T.-W. (2012). Synthesis of large-area MoS_2 atomic layers with chemical vapor deposition. Adv. Mater. *24*, 2320–2325. https://doi.org/10.1002/adma.201104798.
15. Zhou, J., Lin, J., Huang, X., Zhou, Y., Chen, Y., Xia, J., Wang, H., Xie, Y., Yu, H., Lei, J., et al. (2018). A library of atomically thin metal chalcogenides. Nature *556*, 355–359. https://doi.org/10.1038/s41586-018-0008-3.
16. Han, W., Liu, K., Yang, S., Wang, F., Su, J., Jin, B., Li, H., and Zhai, T. (2019). Salt-assisted chemical vapor deposition of two-dimensional materials. Sci. China Chem. *62*, 1300–1311. https://doi.org/10.1007/s11426-019-9525-y.
17. Xie, C., Yang, P., Huan, Y., Cui, F., and Zhang, Y. (2020). Roles of salts in the chemical vapor deposition synthesis of two-dimensional transition metal chalcogenides. Dalton Trans. *49*, 10319–10327. https://doi.org/10.1039/D0DT01561J.
18. Ji, Q., Su, C., Mao, N., Tian, X., Idrobo, J.-C., Miao, J., Tisdale, W.A., Zettl, A., Li, J., and Kong, J. (2021). Revealing the brønsted-evans-polanyi relation in halide-activated fast MoS_2 growth toward millimeter-sized 2D crystals. Sci. Adv. *7*, eabj3274. https://doi.org/10.1126/sciadv.abj3274.
19. Zhu, J., Xu, H., Zou, G., Zhang, W., Chai, R., Choi, J., Wu, J., Liu, H., Shen, G., and Fan, H. (2019). MoS_2-OH bilayer-mediated growth of inch-sized monolayer MoS_2 on arbitrary substrates. J. Am. Chem. Soc. *141*, 5392–5401. https://doi.org/10.1021/jacs.9b00047.
20. Yuan, S., Luo, X., Chan, H.L., Xiao, C., Dai, Y., Xie, M., and Hao, J. (2019). Room-temperature ferroelectricity in $MoTe_2$ down to the atomic monolayer limit. Nat. Commun. *10*, 1775. https://doi.org/10.1038/s41467-019-09669-x.
21. Wang, Y., Xiao, J., Zhu, H., Li, Y., Alsaid, Y., Fong, K.Y., Zhou, Y., Wang, S., Shi, W., Wang, Y., et al. (2017). Structural phase transition in monolayer $MoTe_2$ driven by electrostatic doping. Nature *550*, 487–491. https://doi.org/10.1038/nature24043.
22. Cho, S., Kim, S., Kim, J.H., Zhao, J., Seok, J., Keum, D.H., Baik, J., Choe, D.H., Chang, K.J., Suenaga, K., et al. (2015). Phase patterning for ohmic homojunction contact in $MoTe_2$. Science *349*, 625–628. https://doi.org/10.1126/science.aab3175.
23. Tang, S., Zhang, C., Wong, D., Pedramrazi, Z., Tsai, H.-Z., Jia, C., Moritz, B., Claassen, M., Ryu, H., Kahn, S., et al. (2017). Quantum spin Hall state in monolayer 1T′-WTe_2. Nat. Phys. *13*, 683–687. https://doi.org/10.1038/nphys4174.
24. Sharma, P., Xiang, F.-X., Shao, D.-F., Zhang, D., Tsymbal, E.Y., Hamilton, A.R., and Seidel, J. (2019). A room-temperature ferroelectric semimetal. Sci. Adv. *5*, eaax5080. https://doi.org/10.1126/sciadv.aax5080.
25. Sung, J.H., Heo, H., Si, S., Kim, Y.H., Noh, H.R., Song, K., Kim, J., Lee, C.S., Seo, S.Y., Kim, D.H., et al. (2017). Coplanar semiconductor-metal circuitry defined on few-layer $MoTe_2$ via polymorphic heteroepitaxy. Nat. Nanotechnol. *12*, 1064–1070. https://doi.org/10.1038/nnano.2017.161.
26. Zhang, Q., Wang, X.-F., Shen, S.-H., Lu, Q., Liu, X., Li, H., Zheng, J., Yu, C.-P., Zhong, X., Gu, L., et al. (2019). Simultaneous synthesis and integration of two-dimensional electronic components. Nat. Electron. *2*, 164–170. https://doi.org/10.1038/s41928-019-0233-2.
27. Fei, Z., Zhao, W., Palomaki, T.A., Sun, B., Miller, M.K., Zhao, Z., Yan, J., Xu, X., and Cobden, D.H. (2018). Ferroelectric switching of a two-dimensional metal. Nature *560*, 336–339. https://doi.org/10.1038/s41586-018-0336-3.
28. de la Barrera, S.C., Cao, Q., Gao, Y., Gao, Y., Bheemarasetty, V.S., Yan, J., Mandrus, D.G., Zhu, W., Xiao, D., and Hunt, B.M. (2021). Direct measurement of ferroelectric polarization in a tunable semimetal. Nat. Commun. *12*, 5298. https://doi.org/10.1038/s41467-021-25587-3.
29. Wang, J., Xu, X., Cheng, T., Gu, L., Qiao, R., Liang, Z., Ding, D., Hong, H., Zheng, P., Zhang, Z., et al. (2022). Dual-coupling-guided epitaxial growth of wafer-scale single-crystal WS_2 monolayer on vicinal a-plane sapphire. Nat. Nanotechnol. *17*, 33–38. https://doi.org/10.1038/s41565-021-01004-0.
30. Liu, M., Liao, J., Liu, Y., Li, L., Wen, R., Hou, T., Ji, R., Wang, K., Xing, Z., Zheng, D., et al. (2023). Periodical ripening for MOCVD growth of large 2D transition metal dichalcogenide domains. Adv. Funct. Mater. *33*, 2212773. https://doi.org/10.1002/adfm.202212773.
31. Humphreys, C. (1989). Controlling crystal growth. Nature *341*, 689. https://doi.org/10.1038/341689A0.
32. Zhou, L., Huang, S., Tatsumi, Y., Wu, L., Guo, H., Bie, Y.Q., Ueno, K., Yang, T., Zhu, Y., Kong, J., et al. (2017). Sensitive phonon-based probe for structure identification of 1T′ $MoTe_2$. J. Am. Chem. Soc. *139*, 8396–8399. https://doi.org/10.1021/jacs.7b03445.
33. Ma, L., Zhu, J., Li, W., Huang, R., Wang, X., Guo, J., Choi, J.-H., Lou, Y., Wang, D., and Zou, G. (2021). Immobilized precursor particle driven growth of centimeter-sized $MoTe_2$ monolayer. J. Am. Chem. Soc. *143*, 13314–13324. https://doi.org/10.1021/jacs.1c06250.
34. Chen, K., Chen, Z., Wan, X., Zheng, Z., Xie, F., Chen, W., Gui, X., Chen, H., Xie, W., and Xu, J. (2017). A simple method for synthesis of high-quality millimeter-scale 1T′ transition-metal

telluride and near-field nanooptical properties. Adv. Mater. *29*. https://doi.org/10.1002/adma.201700704.

35. Zhou, J., Liu, F., Lin, J., Huang, X., Xia, J., Zhang, B., Zeng, Q., Wang, H., Zhu, C., Niu, L., et al. (2017). Large-area and high-quality 2D transition metal telluride. Adv. Mater. *29*, 1603471. https://doi.org/10.1002/adma.201603471.

36. Zhuang, P., Sun, Y., Dong, P., Smith, W., Sun, Z., Ge, Y., Pei, Y., Cao, Z., Ajayan, P.M., Shen, J., and Ye, M. (2019). Revisiting the role of active sites for hydrogen evolution reaction through precise defect adjusting. Adv. Funct. Mater. *29*, 1901290. https://doi.org/10.1002/adfm.201901290.

37. Guo, Z., Wang, L., Han, M., Zhao, E., Zhu, L., Guo, W., Tan, J., Liu, B., Chen, X.-Q., and Lin, J. (2022). One-step growth of bilayer 2H-1T′ $MoTe_2$ van der waals heterostructures with interlayer-coupled resonant phonon vibration. ACS Nano *16*, 11268–11277. https://doi.org/10.1021/acsnano.2c04664.

38. Chen, S.-Y., Naylor, C.H., Goldstein, T., Johnson, A.T.C., and Yan, J. (2017). Intrinsic phonon bands in high-quality monolayer T′ molybdenum ditelluride. ACS Nano *11*, 814–820. https://doi.org/10.1021/acsnano.6b07260.

STAR★METHODS

KEY RESOURCES TABLE

REAGENT or RESOURCE	SOURCE	IDENTIFIER
Chemicals, peptides, and recombinant proteins		
Molybdenum pentachloride	Strem Chemicals	CAS: 10241-05-1
Tungsten chloride	Sigma-Aldrich	CAS: 13283-01-7
Tellurium powder	Sigma-Aldrich	CAS: 13494-80-9
Potassium tellurite	Sigma-Aldrich	CAS: 7790-58-1
Polymethyl Methacrylate	Sigma-Aldrich	CAS: 9011-14-7
Acetone	Sinopharm Chemical Reagent Co., China	CAS: 67-64-1
Software and algorithms		
Origin 2018	Origin Lab Corporation	https://www.originlab.com
Cinema 4D	Maxon Computer	https://www.maxon.net

RESOURCE AVAILABILITY

Lead contact

Further information and requests for resources and materials should be directed to and will be fulfilled by the lead contact, Lin Zhou. e-mail: linzhou@sjtu.edu.cn.

Materials availability

This study did not generate new unique reagents.

Data and code availability

- All data reported in this paper in this paper is available from the lead contact upon request.
- This study does not report the original code.
- Any additional information required to reanalyze the data reported in this paper is available from the lead contact upon request.

EXPERIMENTAL MODELS AND STUDY PARTICIPANT DETAILS

Our study does not use experimental models in the life sciences.

METHOD DETAILS

Synthesis and transfer of $MoTe_2$ and WTe_2

High-quality $MoTe_2$ and WTe_2 were synthesized by ambient pressure CVD growth. K_2TeO_3 powder (Sigma-Aldrich, 99.9%) was dissolved in deionized water. The K_2TeO_3 solution was spin-coated on mica substrate at 2000 rpm for 60 s and then baked on a heating plate at 60°C. The $MoCl_5$ (Strem Chemicals, 99.9%) or WCl_6 (Sigma-Aldrich, 99.9%) powder was placed in a quartz boat at the hot zone's edge, where the temperature was ~180°C. The Te powder (Sigma-Aldrich, 99.9%) was placed at the heating center of the tube furnace. Before heating, the CVD system was vacuumed and purged by Ar gas three times to remove water and air. Then, the furnace temperature was ramped to 650°C within 15 min, with a mixture of 250 sccm Ar and 5 sccm H_2 as the carrier gas and maintained at growth temperatures for 3 min. After growth, the quartz tube was removed from the furnace and rapidly cooled to room temperature. Moreover, the as-synthesized $MoTe_2$ or WTe_2 with different thicknesses and sizes can be obtained by adjusting different temperatures and growth times.

The as-grown $MoTe_2$ or WTe_2 were transferred onto target substrate (such as SiO_2/Si substrate and TEM grid) via polystyrene (PMMA)-assisted wet transfer approach for further structure and property characterization. First, the PMMA solution was spin-coated on mica substrate with as-grown $MoTe_2$ or WTe_2 at a speed of 2000 rpm for 60 s and then baked on a heating plate at 120°C for 30 min. Second, the PMMA film with $MoTe_2$ or WTe_2 was delaminated from the mica substrate with water assistance. Then, the target substrate picks up the PMMA film from water. Finally, the target substrate with PMMA film was heated at 120°C for 30 min and then immersed into acetone to remove PMMA.

Structure and spectral characterization

Optical images of $MoTe_2$ and WTe_2 were obtained by optical microscope (OM, Leica DM2700M). AFM (Bruker Multimode 8) was used to characterize the surface morphology and thickness of $MoTe_2$. XPS (Thermo Scientific NEXSA) was carried out to confirm the chemical composition and phase structure of $MoTe_2$. Atomic structure and element distribution were analyzed via high-resolution transmission electron microscopy (HRTEM, FEI Talos F200X) and EDS mapping (TEM, FEI Talos F200X). Raman spectra, Raman mapping, and angle-resolved polarization Raman spectra were acquired on Renishaw inVia Qontor with a 532 nm laser. The chemical composition imaging and depth analysis of $MoTe_2$ were carried out by time-of-flight secondary ion mass spectrometer (ION TOF TOF-SIMS 5100).

QUANTIFICATION AND STATISTICAL ANALYSIS

In Figures 2D and 2E, each thickness and lateral dimension value corresponds to the average value obtained from the measurements of various $MoTe_2$ on a mica substrate.